How to cite: *Angew. Chem. Int. Ed.* **2024**, *63*, e202314181
doi.org/10.1002/anie.202314181

Na-ion Batteries

A Dual Anion Chemistry-Based Superionic Glass Enabling Long-Cycling All-Solid-State Sodium-Ion Batteries

*Xiaoting Lin[+], Yang Zhao[+], Changhong Wang[+], Jing Luo, Jiamin Fu, Biwei Xiao, Yingjie Gao, Weihan Li, Shumin Zhang, Jiabin Xu, Feipeng Yang, Xiaoge Hao, Hui Duan, Yipeng Sun, Jinghua Guo, Yining Huang, and Xueliang Sun**

Abstract: Glassy Na-ion solid-state electrolytes (GNSSEs) are an important group of amorphous SSEs. However, the insufficient ionic conductivity of state-of-the-art GNSSEs at room temperature lessens their promise in the development of all-solid-state Na-ion batteries (ASSNIBs) with high energy density and improved safety. Here we report the discovery of a new sodium superionic glass, $0.5Na_2O_2$-$TaCl_5$ (NTOC), based on dual-anion sublattice of oxychlorides. The unique local structures with abundant bridging and non-bridging oxygen atoms contributes to a highly disordered Na-ion distribution as well as low Na^+ migration barrier within NTOC, enabling an ultrahigh ionic conductivity of 4.62 mS cm^{-1} at 25 °C (more than 20 times higher than those of previously reported GNSSEs). Moreover, the excellent formability of glassy NTOC electrolyte and its high electrochemical oxidative stability ensure a favourable electrolyte-electrode interface, contributing to superior cycling stability of ASSNIBs for over 500 cycles at room temperature. The discovery of glassy NTOC electrolyte would reignite research enthusiasm in superionic glassy SSEs based on multi-anion chemistry.

Introduction

Rechargeable Na-ion batteries have the potential to be a cost-effective solution for grid-scale energy storage owing to the abundance and low cost of sodium.[1] However, the employment of flammable organic liquid electrolytes and their limited energy density pose serious safety concerns and hinder their practical applications.[2] All-solid-state Na-ion batteries (ASSNIBs) have emerged as a promising solution to overcome these challenges by utilizing a solid-state electrolyte (SSE) for higher energy density and improved safety.[3] To enable high-performance ASSNIBs, Na-ion SSEs should possess high ionic conductivity, a wide electrochemical stability window, good device integration capabilities, and superior interfacial compatibility with electrodes.

Over the past decades, various Na-ion SSEs have been developed, such as oxides, sulfides, halides, and polymers.[4] These SSEs can be generally classified into two categories: crystalline and amorphous. Crystalline SSEs have a well-defined, long-range ordered atomic structure. The ions in crystalline SSEs are held in fixed positions and can only move through the well-defined channels or planes.[5] Their ion transport behavior is significantly affected by the concentration of available adjacent positions or defects, the size of the bottleneck of ion transport channels, and the grain boundaries.[4c,6] In contrast, amorphous SSEs lack the long-range periodic ordering of their constituent atoms. The Na^+ ions in amorphous SSEs are randomly distributed and are not restricted by fixed channels or planes.[7] Therefore, amorphous SSEs generally show higher ionic conductivities and softer mechanical properties than their crystalline counterparts, making them more suitable for next-generation all-solid-state batteries.[8]

As a subset of amorphous SSEs, ionic glass appears to be particularly interesting as it has the disordered structure of a liquid yet its physical properties resemble those of a solid.[9] Therefore, glass is customarily considered a "supercooled liquid". Other distinct advantages of glassy SSEs

[*] X. Lin,[+] Y. Zhao,[+] C. Wang,[+] J. Luo, J. Fu, Y. Gao, W. Li, S. Zhang, X. Hao, H. Duan, Y. Sun, X. Sun
Department of Mechanical and Materials Engineering, University of Western Ontario
1151 Richmond St, London, Ontario, N6A 3K7 (Canada)
E-mail: xsun9@uwo.ca

C. Wang,[+] X. Sun
Eastern Institute for Advanced Study, Eastern Institute of Technology
Ningbo, Zhejiang 315200 (P. R. China)

J. Fu, S. Zhang, J. Xu, Y. Huang
Department of Chemistry, University of Western Ontario
1151 Richmond St, London, Ontario, N6A 3K7 (Canada)

B. Xiao
GRINM, Institute for Advanced Materials and Technology
Foshan, Guangdong, 528051 (P. R. China)

F. Yang, J. Guo
Advanced Light Source, Lawrence Berkeley National Laboratory
Berkeley, CA 94720 (USA)

[+] These authors contributed equally to this work.

over their crystalline counterparts include isotropic ionic conduction, the absence of grain boundaries, and the ease of fabricating a thin film. As such, Na^+-ion conducting glass is a perspective class of SSEs that shows immense technological promise in the development of ASSNIBs.[10] Thus far, many oxide- and sulfide-based glassy Na-ion SSEs (GNSSEs) have been reported, such as Na_2O-SiO_2 (2.8×10^{-5} S cm^{-1}, 100 °C),[9a] $0.5Na_2S$-$0.5SiS_2$ (1.2×10^{-5} S cm^{-1}, 25 °C),[11] $0.8Na_2S$-$0.2P_2S_5$ (1×10^{-5} S cm^{-1}, 25 °C),[12] $Na_3Al_2P_3O_{12}$ (3.28×10^{-7} S cm^{-1}, 100 °C),[8b] $90Na_2P_2O_6$-$10Na_2Te_2O_5$ (2.4×10^{-6} S cm^{-1}, 150 °C),[13] $Na_{3.75}Zr_{1.1}Si_{2.75}P_{0.25}O_{10.2}$ (1.9×10^{-3} S cm^{-1}, 300 °C),[14] and $Na_3PS_{4-x}O_x$ (2.7×10^{-4} S cm^{-1}, 60 °C).[8a] Apparently, most previously reported GNSSEs exhibit insufficient ion conductivities, even at elevated temperatures (≈100–300 °C), significantly downplaying their potential and slowing down the progress of ASSNIB's development. On the other hand, it can be noted that most of these GNSSEs are based on single anions, which may set limitations on local glass networks and the resultant Na^+ ion mobility.[9a,15] Therefore, a breakthrough in the ionic conductivity of GNSSEs is highly desired and requires the rational design of new compositional spaces.

In contrast to conventional GNSSEs that are based on a single anion sublattice, here we report a new superionic glass electrolyte, $0.5Na_2O_2$-$TaCl_5$ (NTOC; 450 °C), based on dual anions of oxychlorides. The glassy NTOC matrix is mainly composed of $TaCl_6$ octahedrons, TaO_xCl_y polyhedrons, and oligomeric Ta-centered polyhedrons connecting via corner-shared oxygen, along with highly disordered Na^+ ion distribution. The unique local structures weaken interactions of Na^+ with surroundings, smoothing the way for their long-range migration and contributing to an impressive ionic conductivity of 4.62 mS cm^{-1} at 25 °C. Additionally, the NTOC electrolyte show good compressibility without obvious pores or voids after simply cold pressing, eliminating the need for high temperature and high pressure required for ASSNIB fabrication and operation. When paired with an uncoated high-voltage layered oxide cathode ($Na_{0.85}Mn_{0.5}Ni_{0.4}Fe_{0.1}O_2$), ASSNIBs demonstrate long cycling stability of 500 cycles at 0.1 C at 25 °C. This research brings a breakthrough in the advancement of high-performance ASSNIBs based on superionic glass electrolytes.

Results and Discussion

The dual anion framework of oxychloride is selected for sodium superionic glass because of the long ionic bond length and high polarizability of both Cl^- and O^{2-} anions.[16] The xNa_2O_2-$TaCl_5$ (x = 0.3, 0.4, 0.5, 0.6, and 0.8) compounds were prepared by a co-melting method under vacuum at 450 °C. X-ray diffraction (XRD) patterns of the as-prepared samples are shown in Figure 1a. Optimization of the reagent stoichiometries revealed that a ratio of Na_2O_2:$TaCl_5$ = 0.5:1 was required for relative pure amorphous phase formation, with a negligible amount of NaCl impurity detected. Ratios other than 0.5:1 led to an unknown crystalline phase (x < 0.5) or a higher content of NaCl by-product and excess Na_2O_2 (x > 0.5). However, simply controlling the reagent

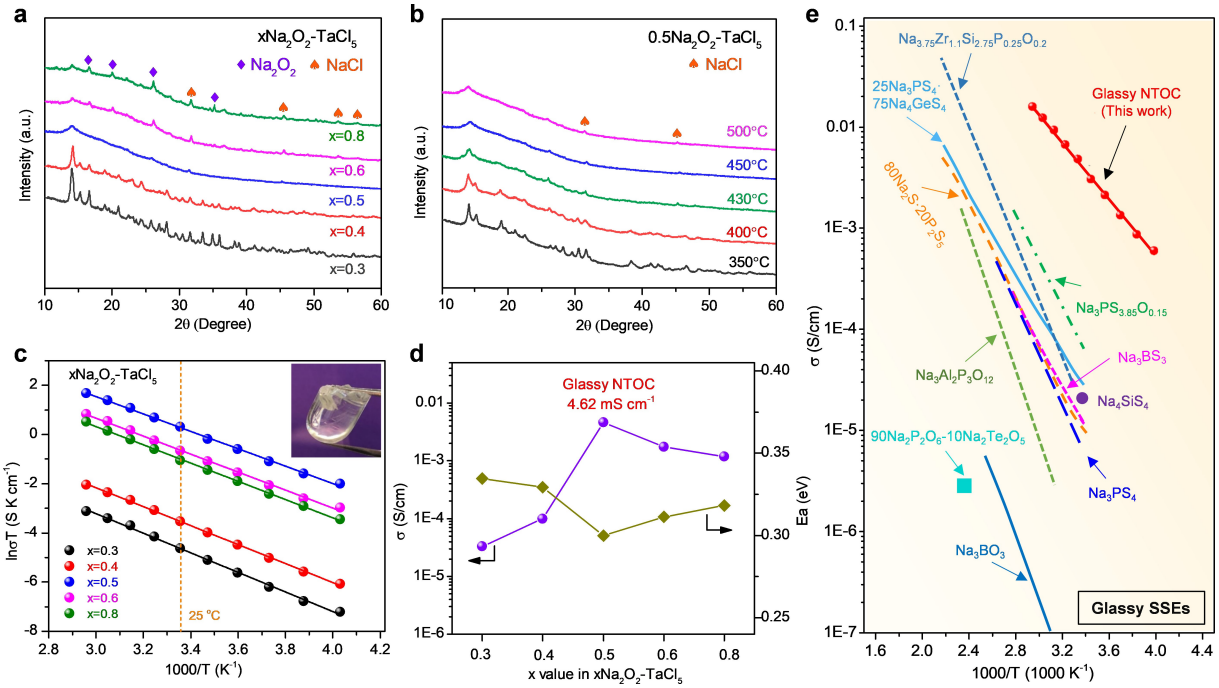

Figure 1. (a) XRD patterns of the xNa_2O_2-$TaCl_5$ (x = 0.3, 0.4, 0.5, 0.6, and 0.8) samples co-melted at 450 °C. (b) XRD patterns of the $0.5Na_2O_2$-$TaCl_5$ samples co-melted at different temperatures. (c) The Arrhenius plots of cold-pressed xNa_2O_2-$TaCl_5$ samples (insert is a photograph of pure bulk NTOC electrolyte). (d) Comparison of RT ionic conductivities and activation energies of xNa_2O_2-$TaCl_5$ (x = 0.3, 0.4, 0.5, 0.6, and 0.8) samples. (e) Summary of the ionic conductivity of glassy Na^+-ion conductors compared with the NTOC electrolyte.

stoichiometries is not sufficient to yield a relatively high-purity amorphous phase; the sintering temperatures and quenching rates were identified as key parameters that affect the phase compositions. As depicted in Figure 1b, diffraction peaks from a second unknown crystalline phase can be observed when the sintering temperature is $\leq 430\,^{\circ}C$, and the relative intensity of characteristic peaks decreases gradually with increasing temperature. It is believed that a high sintering temperature offers a high chemical driving force, and increasing the temperature to 450 °C affords the driving force to form an amorphous $0.5Na_2O_2$-$TaCl_5$ phase. It needs to be pointed out that the disappearance of crystalline characteristic peaks does not mean the simple phase transformation from crystalline to amorphous, since the phase composition changed due to the release of greenish-yellow Cl_2 gas when increasing the temperature to 450 °C (Figure S1). The generation of Cl_2 gas is ascribed to the occurrence of redox reaction which involves the reduction of peroxide ions to divalent oxygen ions and oxidation of Cl^- to Cl_2 gas ($O_2^{2-} + 2Cl^- = Cl_2 \uparrow + 2O^{2-}$). No significant phase changes can be observed as the temperature continues to rise to 550 °C. Additionally, the phase compositions were further measured as a function of cooling rate. Quenching favors the formation of an amorphous phase, and an increasing amount of crystalline impurity can be detected by extending the cooling time (Figure S2). The amorphous 0.5 Na_2O_2-$TaCl_5$ prepared at 450 °C with rapid quenching was used for subsequent studies and denoted as NTOC in the following results.

The thermal behavior of the amorphous NTOC powder was first examined, and the differential scanning calorimetry (DSC) curve reveals that the amorphous NTOC phase is glass. The glass transition temperature (T_g) of the NTOC glass is identified as 147 °C (Figure S3). The optical image of the pure bulk NTOC electrolyte indicates its perfectly transparent glass state (insert in Figure 1c), and the surface of the NTOC was homogeneous and smooth without any visible voids (Figure S4). After a few minutes of manual grinding, the transparent bulk NTOC glass turns into a white powder with micrometer-sized particles (Figure S5). Interestingly, the NTOC electrolyte exhibits outstanding formability. The NTOC powder can be reversibly transformed to a highly dense and poreless appearance after simple cold pressing at ≈ 300 MPa (Figure S6). The energy dispersive spectroscopy (EDS) elemental mapping images indicate the uniform distribution of the Na, Ta, O, and Cl elements across the cold-pressed NTOC pellet (Figure S7). In sharp contrast, voids and grain boundaries are observable for the cold-pressed crystalline $NaTaCl_6$ SSE, even when much higher pressure was applied (Figure S8). Such a mechanical property difference is presumably closely related to the oxygen participation that may play a critical role in the local structures of the NTOC electrolyte.[8a] Overall, for oxychloride NTOC glass, its excellent formability and unique soft nature could favor the solid-solid interfacial contact in ASSNIBs. Meanwhile, the absence of crystalline conduction pathways or particulate interfaces in cold-pressed NTOC SSE contributes to isotropic ion mobility without grain boundary resistance, benefiting fast and continuous Na^+-ion transport.[8a]

The ionic transport behavior of the NTOC electrolyte was then studied. The impedance plot of the NTOC exhibits a semicircle and a spike in the low-frequency region, suggesting that the NTOC behaves as a typical ionic conductor (Figure S9). Arrhenius plots of the xNa_2O_2-$TaCl_5$ with different reagent stoichiometries and the $0.5Na_2O_2$-$TaCl_5$ samples sintered at different temperatures are displayed in Figures 1c and S10, the corresponding ionic conductivities at 25 °C and the activation energies (E_a) are compared in Figure 1d and S11, respectively. It can be clearly observed that the optimized composition of amorphous $0.5Na_2O_2$-$TaCl_5$ (NTOC) exhibits an ultrahigh ionic conductivity of $4.62\,mS\,cm^{-1}$ at 25 °C with the lowest activation energy of 0.30 eV among all samples. Meanwhile, the electronic conductivity of NTOC electrolyte is negligible ($< 10^{-10}\,S\,cm^{-1}$) as measured via direct current polarization, indicative of a good electronic insulator (Figure S12). Since the ionic conductivity of SSEs is highly dependent on their intrinsic structures, it can be inferred that the superionic property of NTOC electrolyte originates from the favorable local structures that enable fast, long-range Na^+ mobility, which will be discussed later. It is noteworthy that the NTOC electrolyte exhibits the highest ionic conductivity among GNSSEs reported so far (Figure 1e). Impressively, the ionic conductivity of NTOC electrolyte is more than 20 times higher than that of the state-of-the-art Na^+-ion conductive glass ($Na_3PS_{4-x}O_x$) reported recently ($0.27\,mS\,cm^{-1}$ at 60 °C).[8a] A summary of the ionic conductivity of the representative inorganic SSEs is also presented in Figure S13. The comparative study further indicates that the ionic conductivity of NTOC electrolytes is superior to that of any reported cold-pressed Na^+-ion conductors. Particularly, the ionic conductivity of NTOC glass is two orders of magnitude higher than recently-revived sodium halides, including Na_2ZrCl_6, $NaAlCl_4$, $NaTaCl_6$, $Na_{3-x}Er_{1-x}Zr_xCl_6$, and $Na_{3-x}Y_{1-x}Zr_xCl_6$.[3b,8c,17] It is to be noted that despite a higher conductivity of $32\,mS\,cm^{-1}$ was achieved for a sintered $Na_{2.88}Sb_{0.88}W_{0.12}S_4$ pellet, the use of glassy NTOC electrolyte in ASSNIBs promises good device integration capabilities by simple cold pressing.[5b]

In addition to good formability and ultrahigh ionic conductivity, this oxychloride NTOC glass also exhibits good chemical stability against dry air. As shown in Figure S14 and S15, no significant changes were observed in both phase compositions and ionic conductivity of the glassy NTOC electrolyte after exposure to dry air for over 3 days, demonstrating its perspective for large-scale practical battery applications. To further reveal the electrochemical stability of the NTOC electrolyte, a linear sweep voltammetry (LSV) test was performed at $0.1\,mV\,S^{-1}$. The LSV curves in Figure S16 reveal the oxidation and reduction voltages of the NTOC electrolyte are approximately 3.92 V and 2.37 V, respectively. Although the NTOC electrolyte cannot be directly paired with $Na_{15}Sn_4$ (or Na) anode due to the formation of a non-passivating interface, the interfacial incompatibility between NTOC and $Na_{15}Sn_4$ electrode can be addressed by inserting a Na_3PS_4 interlayer, which is

promising to facilitate the stabilization of electrolyte/anode interface in NTOC-based ASSNIBs (Figure S17–S18).

Structural analysis of glassy NTOC is necessary to shed light on the correlation between local network structures and the fast Na-ion conduction mechanism. Raman spectra of NTOC show a strong polarized band at 398 cm^{-1} and a depolarized band of medium intensity at 103–184 cm^{-1}, close to the A_{1g} and T_{2g} modes of $TaCl_6^-$ in $NaTaCl_6$, respectively (Figure 2a).[18] It is reasonable to assume that $TaCl_6^-$ units may be present in the glassy NTOC. The high-energy Raman bands at 700–900 cm^{-1} can be ascribed to the coupled modes involving mainly the stretching of bridging oxygen (O-3Ta/O-2Ta) in the NTOC.[18–19] Further evidence of the presence of bridging oxygen, as well as non-bridging oxygen, in the NTOC can be found in the O 1s X-ray photoelectron spectroscopy (XPS) spectra in Figure 2b.[8a] The possible origin of the medium weak band at 215 cm^{-1} is breathing vibrations of Ta polyhedrons where Ta atoms are bonded through bridging oxygen. Consequently, the NTOC may contain many different oligomeric Ta-centered polyhedrons, and the symmetrical stretching of Ta–Cl bonds in the oligomeric polyhedrons should show bands near the frequency of symmetrical stretching of Ta–Cl in $TaCl_6^-$. These bands probably partly overlap with $TaCl_6^-$ at 398 cm^{-1}. In addition, O *K*-edge X-ray absorption spectroscopy (XAS) spectra indicate that NTOC glass essentially contains Ta–O bonds, and the coordination geometry around the O atoms resembles that of O in orthorhombic Ta_2O_5 (Figure S19). Thus, the bridging O atoms in NTOC are expected to be bonded to two equivalent Ta^{5+} atoms in a linear geometry and bonded to three Ta^{5+} atoms in a trigonal planar geometry and/or a distorted geometry, in good agreement with the Raman results.[19c]

The local coordination environment around the Ta atoms in NTOC was further explored by conducting XAS analysis. Figure S20 shows the normalized Ta L_3-edge X-ray absorption near edge structure (XANES) spectra of the NTOC and the references of Ta_2O_5 and $TaCl_5$. The differences in energy position and intensity of the white-line and the resonances suggest their different Ta local environment, which is related to the number and geometrical arrangement of the neighboring Cl and/or O atoms around Ta.[20] The structural properties around the Ta atoms can be more clearly seen in more detail in the extended XAFS (EXAFS) at the Ta L_3-edge. The signals of wavelet-transformed (WT)-EXAFS near 1.5 Å and 2 Å correspond to the nearest neighboring O and Cl atoms around a centered Ta atom, respectively (Figure 2c). Further, the Fourier transformed (FT)-EXAFS fitting results clearly revealed that the average coordination numbers of Ta–O and Ta–Cl were 1.8 and 3.9,

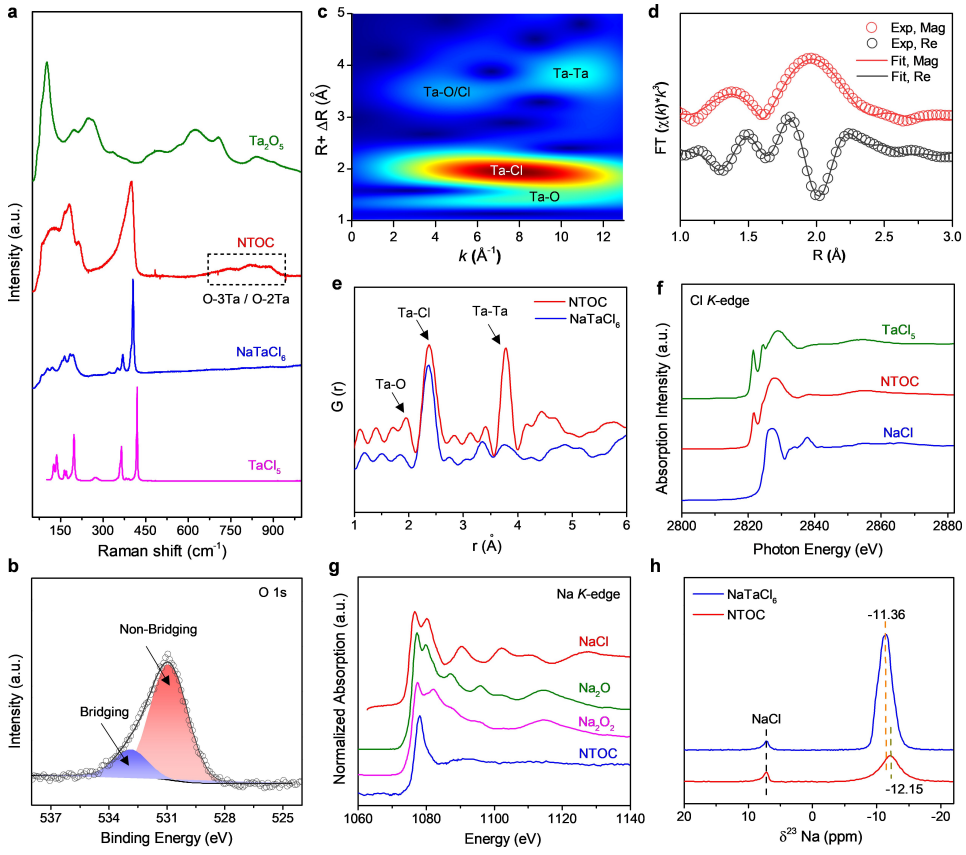

Figure 2. (a) Raman spectra of NTOC and reference samples. (b) O 1s XPS spectrum of NTOC glass electrolyte. (c) WT-EXAFS of NTOC electrolyte at Ta L_3-edge. A k^3 weighting was used. (d) FT-EXAFS fitting results for the Ta L_3-edge spectrum of the NTOC electrolyte. (e) PDF profiles of the NTOC and $NaTaCl_6$ electrolytes. (f) Cl *K*-edge and (g) Na *K*-edge XANES spectra of the NTOC electrolyte and the reference samples. (h) ^{23}Na solid-state NMR spectra of NTOC and $NaTaCl_6$ electrolytes.

respectively, and the detailed coordination information around a centered Ta is summarized in Table S1. WT-EXAFS also provides intuitive information about the second nearest neighbor interactions of Ta-centered polyhedrons, and the results disclose an intensity maxima of Ta–Ta single scattering at around 3.9 Å, validating that the Ta-centered species coordinated with other Ta centers in the medium range. The WT-EXAFS results were corroborated by the pair distribution function (PDF) profile, which implies that the Ta was nearest coordinated with O and Cl atoms in NTOC (Figure 2e). Of note, compared with the $NaTaCl_6$ that is composed of discrete $[TaCl_6]^-$ units, the most distinct feature of NTOC is an intense Ta–Ta peak at ≈3.8 Å, reconfirming the existence of a significant amount of oligomeric Ta-centered frameworks connecting via corner-sharing oxygen.[20–21]

The local configuration around Na atoms is also important since the diffusion of Na^+ through the network is affected by their local coordination and their bonding with the framework.[22] Based on the Cl *K*-edge XAS spectrum in Figure 2f, the Cl in the NTOC electrolyte could be recognized to be mainly coordinated by Ta, without obvious signs of a Na–Cl scattering path. Interestingly, NTOC displays a rather different Na *K*-edge XAS absorption feature from reference samples (Figure 2g). The major features of NTOC are one intense peak at 1078 eV and a smooth resonance around 1091 eV, which are good indications of the local disordering around Na in NTOC glass.[23] In agreement with the high disorder of the sodium environment, a broad featureless resonance was observed at −12.15 ppm in the ^{23}Na solid-state nuclear magnetic resonance (ss NMR) spectrum of NTOC (Figure 2h). Compared with the crystalline $NaTaCl_6$, a slight decrease in chemical shift of the ^{23}Na signal in NTOC reflects the increased number of high-electron-density Ta atoms around Na atoms.[3b,24] This phenomenon further verified the presence of a significant number of oligomeric Ta–O–Cl polyhedrons around Na atoms. It can be thus deduced that Na cations would act as charge compensators near Ta-centered polyhedrons or would be located near non-bridging oxygen.[25] This could explain why the Na atoms in NTOC are free of strong Coulombic attractions from O and Cl in the nearest range.

Taken together, it can be generally concluded that the NTOC glass may mainly constructed from $[TaCl_6]$ octahedrons, $[TaO_xCl_y]$ units, oligomeric Ta-centered polyhedrons connecting via corner-shared oxygen, as well as highly disordered Na^+ ions located around the "random framework" of the glass matrix. In fact, the oxygen incorporation is considered to be responsible for the unique local structures of NTOC and its superionic feature. The explanations for high ionic conductivity of NTOC electrolyte could be proposed as follows. **First**, the existence of non-bridging oxygen in NTOC electrolyte contributes to the formation of a relatively open framework with a large free volume, which permits excellent Na mobility between its initial and final sites.[25] **Second**, non-bridging oxygen also can offer hoping sites for ion conduction where Na^+ jumps into or out easily due to relatively weak bonding or shallow energy well, similar to the function of non-bridging oxygen in oxide glass networks.[26] **Third**, the oxygen corner-sharing connectivity of Ta-centered polyhedrons in NTOC could induce a distorted sodium-site environment and allow for percolating pathways through which sodium can be transported with a low energy barrier.[22b,27] Although the precise structure of the glassy NTOC electrolyte was not disclosed, the oxychloride chemistry was proven to benefit fast Na^+ diffusion in GNSSEs, and the complex interplay of ion-network interactions in NTOC is being investigated in ongoing studies in our laboratory.

With an ultrahigh ionic conductivity, negligible electronic conductivity, high oxidation stability, and good formability, the glassy NTOC is a promising candidate SSE for ASSNIBs. As a proof-of-concept, the glassy NTOC SSE was directly integrated as the solid electrolyte into ASSNIBs with an uncoated high-voltage cathode of $Na_{0.85}Mn_{0.5}Ni_{0.4}Fe_{0.1}O_2$ (NMNFO) and a $Na_{15}Sn_4$ anode; a thin layer of Na_3PS_4 was inserted between NTOC and $Na_{15}Sn_4$ to prevent the undesirable reactions (Figure 3a). In this work, the ASSNIBs were constructed by simply cold pressing at room temperature. The charge-discharge curves and rate performance of ASSNIBs at different current densities ranging from 0.1 C to 1 C ($1\,C = 120\,mA\,g^{-1}$) at room temperature are shown in Figure 3b and c. Reversible discharge capacities of 106.3, 95.4, and 62.3 $mAh\,g^{-1}$ can be delivered at 0.1, 0.2, and 0.3 C between 2.5 and 3.8 V, respectively. Although the capacity gradually decreases along with an increase in current densities, the reversible capacity can be recovered upon returning to 0.1 C. It is important to note that the insufficient ionic conductivity of the Na_3PS_4 interlayer ($\approx 0.1\,mS\,cm^{-1}$) in ASSNIB is partially responsible for the limited capacity of as-developed ASSNIB, especially at high rates. The cycling performance and Coulombic efficiency of the ASSNIB cell at 0.1 C are shown in Figure 3d and e. Surprisingly, the ASSNIB exhibits stable cycling and slow capacity fading at 0.1 C, maintaining 66 % capacity retention over 500 cycles. The overlapping of the oxidation and reduction peaks in cyclic voltammetry (CV) profiles further implies that the NMNFO cathode has good electrochemical reversibility in NTOC-based ASSNIBs (Figure S21).

A galvanostatic intermittent titration technique (GITT) was performed to roughly determine the Na^+ diffusion behaviors in the NMNFO cathode at different electrochemical states of ASSNIB. Figure 3f shows the GITT profile of the ASSNIB at $20\,mA\,g^{-1}$. It can be clearly observed that almost all the electrochemical polarization of NMNFO cathode is less than 50 mV, demonstrating the favorable electrochemical process. The significant increase of polarization at 3.3 V ($\approx 85\,mAh\,g^{-1}$) during charging can be attributed to the structural transition from O3-NMNFO to P3-NMNFO phase, and the gradual increase of polarization during discharging is associated with the gradual saturation of Na^+ sites in the NNMFO crystal structure.[28] The D_{Na+} is further calculated based on the charge and discharge process, as plotted in Figure 3g. The average D_{Na+} values during the charge and discharge processes are 1.093×10^{-12} and $1.059\times10^{-12}\,cm^2\,S^{-1}$, respectively. This result

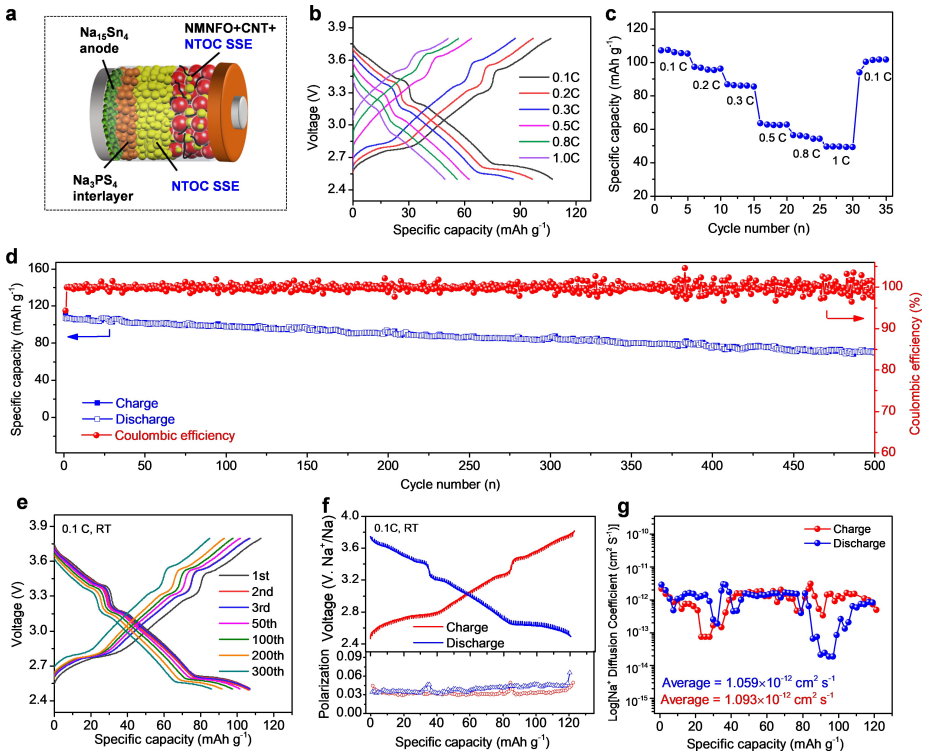

Figure 3. (a) Schematic diagram of NTOC-based ASSNIBs. (b, c) Charge-discharge profiles and rate performance of ASSNIB at different current densities. (d, e) Charge-discharge profiles and cycling performance of ASSNIB at 0.1 C, RT. (f) GITT curve and corresponding polarization curves of the ASSNIB in the initial cycle. 20 mA g^{-1} current pulses are used for 5 min increments followed by 2 h relaxation during GITT testing. (g) Na^+ diffusion coefficients of ASSNIB at different charge-discharge states during the initial cycle.

is consistent with the smaller voltage hysteresis during charging than discharging process, suggesting relatively more feasible reaction kinetics during Na^+ extraction.

Clearly, the ASSNIBs using the NTOC glass SSE demonstrate superior electrochemical performance in terms of fast Na^+ ion diffusion, high reversible capacity, and good cycling stability at room temperature. To the best of our knowledge, this is one of the best electrochemical performance of room-temperature ASSNIBs ever reported in the literature.[8a,29] The good electrochemical performance of ASSNIBs developed in this work is associated with several contributing factors. On one hand, the highly deformable oxychloride NTOC glass electrolyte enables the effective formation of continuous sodium-ion conduction pathways in the ASSNIBs. A cross-sectional SEM image of the composite cathode layer is shown in Figure 4b, it can be clearly observed that the NMNFO cathode particles are embedded into the deformed NTOC electrolyte without significant voids and the surface/edge of the active materials are almost fully covered. The excellent deformable property of the NTOC glassy SSE is also capable of addressing the interfacial contact issues between different cell components. As shown in Figures 4a, 4c, and Figure S22, intimate cathode/NTOC electrolyte and NTOC/Na_3PS_4 interfacial contact can be simultaneously achieved by simple cold pressing at ≈300 MPa, contributing to the formation of effective ionic paths. On the other hand, good chemical/electrochemical compatibility between NTOC electrolyte and NMNFO cathode materials was verified by ex situ XPS analysis on the NTOC interface with NMNFO cathode at different electrochemical states. As shown in Figure 4d and e, no obvious change in the chemistry of NTOC was observed in the Cl 2p and Ta 4f XPS spectra. Furthermore, the Ta L_3-edge and Cl K-edge XANES spectra for cathode composite at different charge/discharge states were essentially unchanged (Figure 4f and 4g). Therefore, the excellent chemical and electrochemical stabilities of the NTOC electrolyte with the uncoated layered oxide NMNFO cathode were confirmed.

Conclusion

In summary, we report a new Na-ion superionic conductor $0.5Na_2O_2$-$TaCl_5$ (NTOC) based on the unique dual-anion sublattice of oxychlorides. The glassy NTOC electrolyte exhibits an ultrahigh ionic conductivity of 4.62×10^{-3} S cm^{-1}, which is more than 20 times higher than previously reported glassy Na-ion SSEs. Such high ionic conductivity mainly originates from the low Coulombic interactions between Na^+-ion and its dual-anion environment of oxychlorides and the specific functions of bridging and non-bridging oxygens. Moreover, the oxychloride framework led to malleable property of NTOC to construct cold-pressed pellets that are free of voids and highly stable at high voltage. The elimination of high-temperature fabrication of all-solid-state

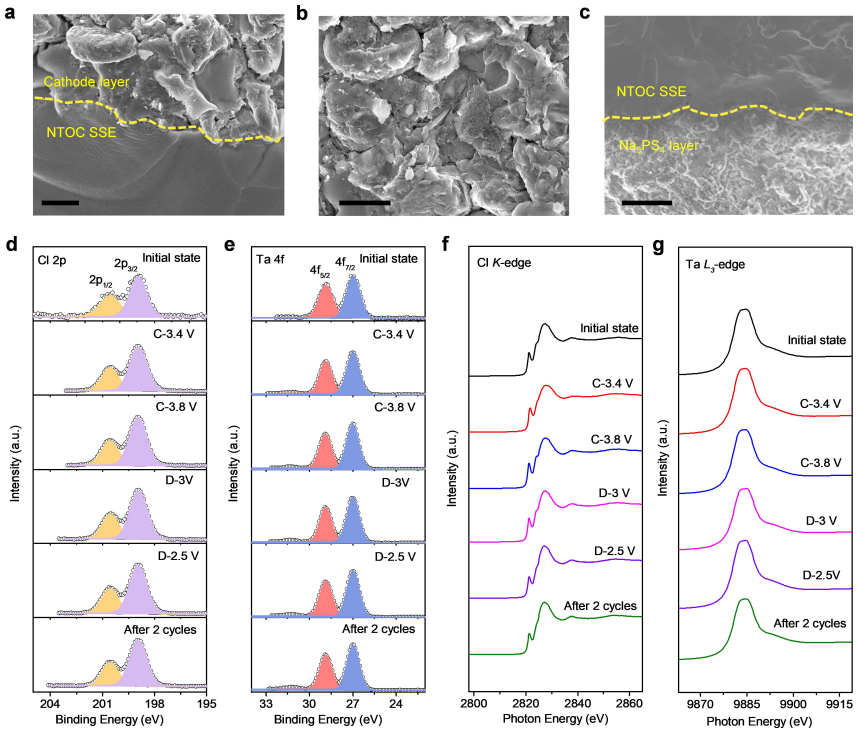

Figure 4. The cross-sectional SEM images of (a) the interphase between the cathode composite layer and NTOC electrolyte, (b) the cathode composite layer, and (c) the interphase between the NTOC electrolyte and Na_3PS_4 layer. The scale bars in a-c are 1 μm. Ex situ (d) Cl 2p and (e) Ta 4 f XPS spectra of cathode composite at different charge/discharge states. (f) Cl *K*-edge and (g) Ta L_3-edge XANES spectra of cathode composite at different charge/discharge states.

Na-ion batteries is manufacturing favorable and environmentally friendly. Using the glassy NTOC as the solid-state electrolytes and an uncoated high voltage layered oxide $Na_{0.85}Mn_{0.5}Ni_{0.4}Fe_{0.1}O_2$ as the cathode, ASSNIBs demonstrate long cycling stability of 500 cycles at 0.1 C at room temperature. This research represents a significant leap in glassy Na-ion solid-state electrolytes and their high-energy-density all-solid-state batteries.

Acknowledgements

This work was supported by the Natural Sciences and Engineering Research Council of Canada (NSERC), the Canada Research Chair Program (CRC), the Canada Foundation for Innovation (CFI), the Ontario Research Fund, and the University of Western Ontario. This research used resources of BL7.3.1 of the Advanced Light Source, which is a DOE Office of Science User Facility under contract no. DE-AC02-05CH11231. Dr. C. Wang, Dr. W. Li, and Dr. J. Fu thanks the support from Mitacs Accelerate Fellowships.

Conflict of Interest

All other authors declare they have no competing interests.

Data Availability Statement

The data that support the findings of this study are available in the supplementary material of this article.

Keywords: All-Solid-State Sodium-Ion Batteries · Glassy Na-Ion Solid-State Electrolytes · Oxychloride · Superionic Glass

[1] a) P.-F. Wang, H.-R. Yao, X.-Y. Liu, Y.-X. Yin, J.-N. Zhang, Y. Wen, X. Yu, L. Gu, Y.-G. Guo, *Sci. Adv.* **2018**, *4*, eaar6018; b) J.-Y. Hwang, S.-T. Myung, Y.-K. Sun, *Chem. Soc. Rev.* **2017**, *46*, 3529–3614.

[2] a) P. Adelhelm, P. Hartmann, C. L. Bender, M. Busche, C. Eufinger, J. Janek, *Beilstein J. Nanotechnol.* **2015**, *6*, 1016–1055; b) A. Hayashi, K. Noi, A. Sakuda, M. Tatsumisago, *Nat. Commun.* **2012**, *3*, 856.

[3] a) H.-L. Yang, B.-W. Zhang, K. Konstantinov, Y.-X. Wang, H.-K. Liu, S.-X. Dou, *Adv. Energy Sustainability Res.* **2021**, *2*, 2000057; b) E. A. Wu, S. Banerjee, H. Tang, P. M. Richardson, J.-M. Doux, J. Qi, Z. Zhu, A. Grenier, Y. Li, E. Zhao, G. Deysher, E. Sebti, H. Nguyen, R. Stephens, G. Verbist, K. W. Chapman, R. J. Clément, A. Banerjee, Y. S. Meng, S. P. Ong, *Nat. Commun.* **2021**, *12*, 1256.

[4] a) Z. Li, P. Liu, K. Zhu, Z. Zhang, Y. Si, Y. Wang, L. Jiao, *Energy Fuels* **2021**, *35*, 9063–9079; b) C. Zhao, L. Liu, X. Qi, Y. Lu, F. Wu, J. Zhao, Y. Yu, Y.-S. Hu, L. Chen, *Adv. Energy Mater.* **2018**, *8*, 1703012; c) J.-F. Wu, R. Zhang, Q.-F. Fu, J.-S. Zhang, X.-Y. Zhou, P. Gao, C.-H. Xu, J. Liu, X. Guo, *Adv. Funct. Mater.* **2021**, *31*, 2008165.

[5] a) Z. Zhang, E. Ramos, F. Lalère, A. Assoud, K. Kaup, P. Hartman, L. F. Nazar, *Energy Environ. Sci.* **2018**, *11*, 87–93; b) A. Hayashi, N. Masuzawa, S. Yubuchi, F. Tsuji, C. Hotehama, A. Sakuda, M. Tatsumisago, *Nat. Commun.* **2019**, *10*, 5266; c) Y. Li, M. Li, Z. Sun, Q. Ni, H. Jin, Y. Zhao, *Energy Storage Mater.* **2023**, *56*, 582–599.
[6] a) Y. Lu, L. Li, Q. Zhang, Z. Niu, J. Chen, *Joule* **2018**, *2*, 1747–1770; b) W. Zhou, Y. Li, S. Xin, J. B. Goodenough, *ACS Cent. Sci.* **2017**, *3*, 52–57; c) X. Lin, Q. Sun, K. Doyle Davis, R. Li, X. Sun, *Carbon Energy* 141–164.
[7] a) J. L. Souquet, *Annu. Rev. Mater. Sci.* **1981**, *11*, 211–231; b) C. A. Angell, *Annu. Rev. Phys. Chem.* **1992**, *43*, 693–717; c) C. A. Angell, *Solid State Ionics* **1983**, *9–10*, 3–16.
[8] a) X. Chi, Y. Zhang, F. Hao, S. Kmiec, H. Dong, R. Xu, K. Zhao, Q. Ai, T. Terlier, L. Wang, L. Zhao, L. Guo, J. Lou, H. L. Xin, S. W. Martin, Y. Yao, *Nat. Commun.* **2022**, *13*, 2854; b) S. R. Keshri, S. Ganisetti, R. Kumar, A. Gaddam, K. Illath, T. G. Ajithkumar, S. Balaji, K. Annapurna, N. Nasani, N. M. A. Krishnan, A. R. Allu, *Inorg. Chem.* **2021**, *60*, 12893–12905; c) H. Kwak, J. Lyoo, J. Park, Y. Han, R. Asakura, A. Remhof, C. Battaglia, H. Kim, S.-T. Hong, Y. S. Jung, *Energy Storage Mater.* **2021**, *37*, 47–54.
[9] a) A. Chandra, A. Bhatt, A. Chandra, *J. Mater. Sci. Technol.* **2013**, *29*, 193–208; b) H. Kitaura, A. Hayashi, T. Ohtomo, S. Hama, M. Tatsumisago, *J. Mater. Chem.* **2011**, *21*, 118–124.
[10] a) R. C. Agrawal, R. K. Gupta, *J. Mater. Sci.* **1999**, *34*, 1131–1162; b) Z. A. Grady, C. J. Wilkinson, C. A. Randall, J. C. Mauro, *Front. Energy Res.* **2020**, *8*.
[11] M. Ribes, B. Barrau, J. L. Souquet, *J. Non-Cryst. Solids* **1980**, *38–39*, 271–276.
[12] K. Noi, A. Hayashi, M. Tatsumisago, *J. Power Sources* **2014**, *269*, 260–265.
[13] G. D. L. K. Jayasinghe, P. W. S. K. Bandaranayake, J. L. Souquet, *Solid State Ionics* **1996**, *86–88*, 447–451.
[14] S. Susman, C. J. Delbecq, J. A. McMillan, M. F. Roche, *Solid State Ionics* **1983**, *9–10*, 667–673.
[15] A. Bunde, K. Funke, M. D. Ingram, *Solid State Ionics* **1998**, *105*, 1–13.
[16] T. Asano, A. Sakai, S. Ouchi, M. Sakaida, A. Miyazaki, S. Hasegawa, *Adv. Mater.* **2018**, *30*, 1803075.
[17] R. Schlem, A. Banik, M. Eckardt, M. Zobel, W. G. Zeier, *ACS Appl. Energ. Mater.* **2020**, *3*, 10164–10173.
[18] T. Xie, W. Brockner, M. Gjikaj, *Z. Anorg. Allg. Chem.* **2010**, *636*, 2633–2640.
[19] a) O. B. Babushkina, S. Ekres, G. E. Nauer, *Z. Naturforsch. A* **2008**, *63*, 73–80; b) O. B. Babushkina, S. Ekres, G. E. Nauer, *J. Phys. Chem. A* **2008**, *112*, 8288–8294; c) C. Joseph, P. Bourson, M. D. Fontana, *J. Raman Spectrosc.* **2012**, *43*, 1146–1150.
[20] Y. R. Denny, T. Firmansyah, S. K. Oh, H. J. Kang, D.-S. Yang, S. Heo, J. Chung, J. C. Lee, *Mater. Res. Bull.* **2016**, *82*, 1–6.
[21] A. Wedig, M. Luebben, D.-Y. Cho, M. Moors, K. Skaja, V. Rana, T. Hasegawa, K. K. Adepalli, B. Yildiz, R. Waser, I. Valov, *Nat. Nanotechnol.* **2016**, *11*, 67–74.
[22] a) S. Houde-Walter, J. Inman, A. Dent, G. Greaves, *J. Phys. Chem.* **1993**, *97*, 9330–9336; b) J. Lee, A. Urban, X. Li, D. Su, G. Hautier, G. Ceder, *Science* **2014**, *343*, 519–522.
[23] D. R. Neuville, L. Cormier, A.-M. Flank, R. J. Prado, P. Lagarde, *Eur. J. Mineral.* **2004**, *16*, 809–816.
[24] C. J. Jameson, *Annu. Rev. Phys. Chem.* **1996**, *47*, 135–169.
[25] D. Caurant, O. Majérus, E. Fadel, A. Quintas, C. Gervais, T. Charpentier, D. Neuville, *J. Nucl. Mater.* **2010**, *396*, 94–101.
[26] a) L. Skuja, *J. Non-Cryst. Solids* **1998**, *239*, 16–48; b) F. H. A. Elbatal, M. A. Marzouk, Y. M. Hamdy, H. A. ElBatal, *J. Solid State Phys.* **2014**, *2014*, 389543.
[27] a) K. Jun, Y. Sun, Y. Xiao, Y. Zeng, R. Kim, H. Kim, L. J. Miara, D. Im, Y. Wang, G. Ceder, *Nat. Mater.* **2022**, *21*, 924–931; b) T. Minami, A. Hayashi, M. Tatsumisago, *Solid State Ionics* **2006**, *177*, 2715–2720; c) M. D. Ingram, *Curr. Opin. Solid State Mater. Sci.* **1997**, *2*, 399–404.
[28] B. Xiao, X. Liu, M. Song, X. Yang, F. Omenya, S. Feng, V. Sprenkle, K. Amine, G. Xu, X. Li, D. Reed, *Nano Energy* **2021**, *89*, 106371.
[29] a) L. Duchêne, R. S. Kühnel, E. Stilp, E. Cuervo Reyes, A. Remhof, H. Hagemann, C. Battaglia, *Energy Environ. Sci.* **2017**, *10*, 2609–2615; b) A. Banerjee, K. H. Park, J. W. Heo, Y. J. Nam, C. K. Moon, S. M. Oh, S.-T. Hong, Y. S. Jung, *Angew. Chem. Int. Ed.* **2016**, *55*, 9634–9638; c) H. Wan, J. P. Mwizerwa, X. Qi, X. Liu, X. Xu, H. Li, Y.-S. Hu, X. Yao, *ACS Nano* **2018**, *12*, 2809–2817; d) S. Zhang, Y. Zhao, F. Zhao, L. Zhang, C. Wang, X. Li, J. Liang, W. Li, Q. Sun, C. Yu, J. Luo, K. Doyle-Davis, R. Li, T.-K. Sham, X. Sun, *Adv. Funct. Mater.* **2020**, *30*, 2001118; e) H. Wan, J. P. Mwizerwa, X. Qi, X. Xu, H. Li, Q. Zhang, L. Cai, Y.-S. Hu, X. Yao, *ACS Appl. Mater. Interfaces* **2018**, *10*, 12300–12304; f) J. W. Heo, A. Banerjee, K. H. Park, Y. S. Jung, S.-T. Hong, *Adv. Energy Mater.* **2018**, *8*, 1702716; g) F. Murgia, M. Brighi, R. Černý, *Electrochem. Commun.* **2019**, *106*, 106534; h) A. L. Santhosha, L. Medenbach, T. Palaniselvam, P. Adelhelm, *J. Phys. Chem. C* **2020**, *124*, 10298–10305; i) D. Zhang, X. Cao, D. Xu, N. Wang, C. Yu, W. Hu, X. Yan, J. Mi, B. Wen, L. Wang, L. Zhang, *Electrochim. Acta* **2018**, *259*, 100–109; j) X. Chi, Y. Liang, F. Hao, Y. Zhang, J. Whiteley, H. Dong, P. Hu, S. Lee, Y. Yao, *Angew. Chem. Int. Ed.* **2018**, *57*, 2630–2634; k) F. Hao, X. Chi, Y. Liang, Y. Zhang, R. Xu, H. Guo, T. Terlier, H. Dong, K. Zhao, J. Lou, Y. Yao, *Joule* **2019**, *3*, 1349–1359; l) C. K. Moon, H.-J. Lee, K. H. Park, H. Kwak, J. W. Heo, K. Choi, H. Yang, M.-S. Kim, S.-T. Hong, J. H. Lee, Y. S. Jung, *ACS Energy Lett.* **2018**, *3*, 2504–2512.

Manuscript received: September 21, 2023
Accepted manuscript online: November 27, 2023
Version of record online: December 11, 2023